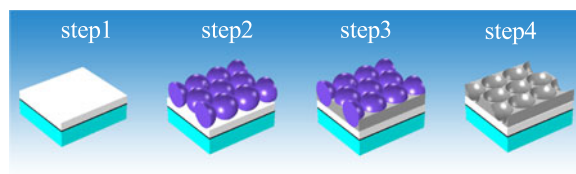


# Influence of Nanovoids Depth on the Surface Magneto-Optical Kerr Effect Modulations in Magnetic Photonic Crystal Slab


Volume 9, Number 6, December 2017

Xia Zhang  
Jing Li  
Yunjie Xia  
Ke Cao  
Xu Zhang  
Yuying Wang  
Xuebo Sun



DOI: 10.1109/JPHOT.2017.2763603  
1943-0655 © 2017 IEEE

# Influence of Nanovoids Depth on the Surface Magneto-Optical Kerr Effect Modulations in Magnetic Photonic Crystal Slab

Xia Zhang <sup>1</sup>, Jing Li,<sup>2</sup> Yunjie Xia,<sup>1</sup> Ke Cao,<sup>1</sup> Xu Zhang,<sup>1</sup>  
Yuying Wang,<sup>1</sup> and Xuebo Sun<sup>1</sup>

<sup>1</sup>Shandong Province Key Lab of Laser Polarization and Information, Qufu Normal University, Qufu 273165, China

<sup>2</sup>Department of Optical Science and Engineering, Fudan University, Shanghai 200433, China

DOI:10.1109/JPHOT.2017.2763603

1943-0655 © 2017 IEEE. Translations and content mining are permitted for academic research only. Personal use is also permitted, but republication/redistribution requires IEEE permission. See [http://www.ieee.org/publications\\_standards/publications/rights/index.html](http://www.ieee.org/publications_standards/publications/rights/index.html) for more information.

Manuscript received September 18, 2017; revised October 9, 2017; accepted October 12, 2017. Date of publication October 16, 2017; date of current version October 31, 2017. This work was supported in part by Shandong Province Natural Science Foundation of China under Grant ZR2015AM024 and in part by Doctoral Research Started Funding of Qufu Normal University under Grant BSQD20130152. Corresponding author: Xia Zhang (e-mail: xzhangqf@mail.qfnu.edu.cn).

**Abstract:** Magnetic photonic crystal slab with nanovoids buried in Ni films were fabricated using nanosphere lithography combined with electrochemical deposition. One featured structure was dominated the spectra of polar surface magneto-optical Kerr effect (MOKE) of samples with different voids depth. For the shallow ones, surface lattice resonance (SLR) was revealed through angle resolved spectra analysis, where the location of degeneracy points corresponded to that of the featured structure in MOKE signal. For the deeper ones, localized plasmons and degeneracy points were all demonstrated in angle resolved reflection spectra, where localized plasmons dominated the resonant MOKE signal, and the degeneracy points blue-shifted compared with that of shallow ones. Changing the lattice of samples, similar phenomena were presented. The physical mechanism of SLR could be attributed to the diffraction of surface plasmons by the reciprocity vector, and the localized plasmons were attributed to the Mie scattering. The featured structure in polar MOKE spectra demonstrated high sensitivity, which might pave the way to on-chip MO devices.

**Index Terms:** Nanosphere lithography, MOKE, ARPS, SLR, localized plasmons.

## 1. Introduction

Analogue with the development of photonic crystals, magnetic photonic crystals (MPC) slab [1]–[3], possessing both the optical and magnetic properties, has attracted much attention because of their intriguing physical properties and important applications in wireless telegraphy [4], [5], integrated photonics [6], nonlinear optics [7], medicine [8], and biosensors [9], [10], etc. Surface Magneto-optical Kerr effect (MOKE), based on polarization conversion detection, is very sensitive and important parameter used in MO device as related above. In traditional ferromagnetic materials, MOKE signal was very weak, which limited its applications, and enhancement of MOKE has been always the issue what researchers have been pursuing. In case of MOKE signal optical

modulation, previous studies revealed that it could be attributed to three issues [11]: (i) substrate effect, (ii) interference effect, and (iii) plasma-edge effect. The physical mechanism about these three effect has been attributed to diagonal components of the dielectric permittivity tensor  $\tilde{\epsilon}_{xx}$  [11], [12], [35], which denote that the magneto-optical activity is related to the electromagnetic field (EF) distribution.

Magnetic photonic crystals slab, possessing small volume (compared with MPC), low loss (including low ferromagnetic material), and easy fabrication, is suitable for MO devices. Both optical and magnetic properties of MPC slab have been characterized through MOKE studies [13], [14]. Surface plasma plasmons (SPP) can be excited in MPC slab [15], which may propagate or localize at the metal-dielectric interface, or combine with other optical modes, such as cavity mode, waveguide mode, and Bragg resonance in photonic crystals. Due to the introduction of both guide mode and cavity mode, enhanced MOKE and high-Q factor had been demonstrated in magnetoplasmonic structures [16]. SPP possess amazing ability to manipulate the EF, such as confining it in small volume, introducing, conducting, and channeling it arbitrarily [17]–[19], as a result, the density of state be controlled and the effective permittivity  $\tilde{\epsilon}_{xx}$  of the system be altered. In MPC slab, surface lattice resonance occurred due to SPP combined with Bragg scattering introduced by the periodic geometry. Thus, MOKE could be modulated by SPP in multi-freedom, exotic properties had demonstrated in MOKE signal in MPC slab [20]–[22]. By changing the 2D lattice, modulated MOKE signal were revealed in magnetic nanoparticle arrays due to the coupling between the plasmonic SLR in x and y-perpendicular direction [23]. In duplex lattice with ferromagnetic and noble metal nanoparticles, diffractive far field coupling between the hybrid lattices resulted in strong magneto-optical activity [24]. Owing to the coupling between the localized plasmons and SLR, resonant enhanced Kerr effect was acquired [25]. In elaborately designed pure ferromagnetic magneto-plasmonic system, strongly tuned MOKE signal was demonstrated due to Fano resonance by coupling between the localized plasmons and SLR [26].

As refer to SPP and other optical modes characterizing, angle resolved spectroscopy (ARPS) is powerful method [27]. From ARPS, the reciprocal space information can be acquired, because it was related to the momentum matching condition needed in SPP generation [15]. And MOKE modulated in MPC slab by optical modes can be elucidated through ARPS analyzing. The MOKE activity of Ni anti-dot arrays had been studied by ARPS, the influence of the geometry symmetry combined with surface plasmons on the MOKE signal was demonstrated [28]. In general, for the ARPS detection method, samples with large areas were required.

Recently, by aids of the hexagonal close-packed PSS template, we fabricated large area planar MPC, hybrid optical modes had been revealed in system with Co nanovoids arrayed on Ag substrate, and resonant MOKE signals acquired, high sensitivity had been proposed in these nanostructured ferromagnetic system [29]. In this paper, the preceding study was performed about the planar MPC. The motivation was as follows: the first was to study the impact of ferromagnetic materials by substituting Ni for Co. The other was to explore the MOKE enhanced by the localized SPP in deepen nano-cavities and the surface lattice resonance scattered by the deepen nanovoids arrays, when the thickness of Ni surpass half of spheres. Based on these motivation, Ni nanovoids with different depth and lattice were fabricated on Ag substrate using the same steps as that of Co nanovoids [29], the polar MOKE were measured and analyzed, and the physical mechanism of the MOKE signal were studied through analysis of angle-resolved reflection spectra.

## 2. Materials and Methods

Ni nano-voids on glass/Ag (150 nm) films were fabricated using nanosphere lithography (NSL) combined with electrochemical deposition. The fabrication steps were displayed in Fig. 1(a) as that in ref [29]. Firstly, Ag films were prepared on glass by dc magnetron sputtering Ag targets, which had two-fold usage as hampering light transmission and as electrode in step 3. Then, the hexagonal lattice templates were synthesized with polystyrene spheres (PSS) self-assembled onto the Ag films as denoted in the step 2, and for the details could be referred to [29]. In step 3, Ni films were deposited into the interstices of PS spheres templates formed in step 2 from Ni aqueous electrolyte

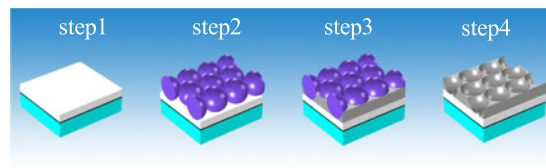


Fig. 1. The schematic plot of fabrication course.

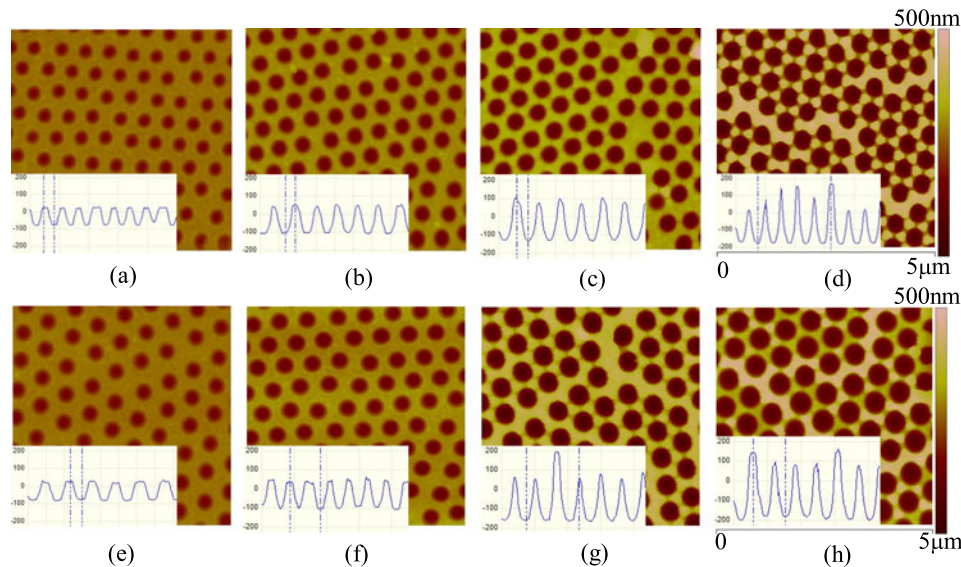


Fig. 2. Top-view of AFM images of samples with lattice (a-d)  $\Lambda = 530$  nm and (e-h)  $\Lambda = 620$  nm. The deposition times (a, e)  $t = 60$  s, (b, f) 100 s, (c, g) 200 s, and (d, h) 300 s, respectively.

by electrochemical deposition, where three-electrode method was performed, the templates were used as the working electrode, Pt wire as counter electrode, and Ag/AgCl as reference electrode. At last, the PSSs were dissolved in the tetrahydrofuran and acetone by sonication for 30 minutes at temperature below  $30^\circ$  alternately. And thus Ni nanovoids were formed on Ag substrate. To avoid the ferromagnetic material oxidation,  $\text{SiO}_2$  films with 3 nanometers were deposited on the nanovoids by electron beam evaporation. In the course of fabrication, we changed deposition time from 60 s to 300 s referred to our former work [29], both shallow voids and deep ones were all obtained. To demonstrate the SLR impact, we fabricated samples with two lattices as  $\Lambda = 530$  nm and  $\Lambda = 620$  nm, respectively.

The morphologies of all samples were characterized by a commercial Atomic force microscopy (AFM) (Sloer P47, NT-MDT). Fig. 2(a)–(d) and (e)–(h) showed morphologies of samples with lattice  $\Lambda = 530$  nm and 620 nm, respectively, where the deposition time were  $t = 60, 100, 200,$  and 300 s for samples (a–d) and (e–h) in turn. The depth were denoted by the inset plots as could be seen in all figures, and were listed out in Table 1 for  $\Lambda = 530$  and Table 2 for  $\Lambda = 620$  nm. Clearly, the depth deepened with enlarging the deposition time.

Polar magneto-optical Kerr rotation  $\theta_k$  and ellipticity  $\varepsilon_k$  were measured at room temperature by home-made Kerr spectrometer from 300 nm to 800 nm, with the incident angle of  $5^\circ$  under the eternal magnetic field of 1.0 T [29]. To analysis the optical modes in these system, angle-resolved reflectivity measurement was performed on home-made spectrometer from 200 nm to 1000 nm, with the incident angle varied from  $-60^\circ$  to  $60^\circ$ . In the reflectivity measurements, the data was normalized with respect to that of Al films.

TABLE 1  
Hole Depth of Samples With  $\Lambda = 530$  nm

No.	(a)	(b)	(c)	(d)
530	100 nm	157 nm	230 nm	340 nm

TABLE 2  
Hole Depth of Samples With  $\Lambda = 620$  nm

No.	(e)	(f)	(g)	(h)
620	101 nm	140 nm	318 nm	350 nm

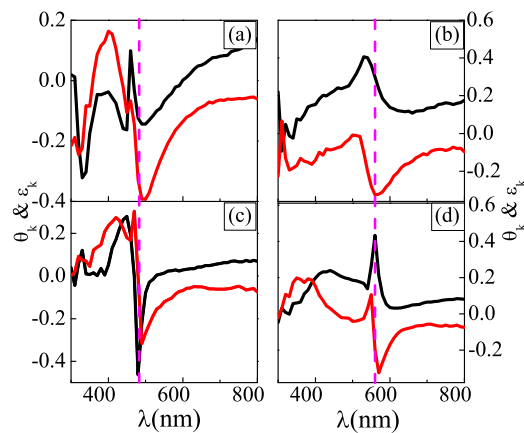


Fig. 3. Comparison of MOKE signal as function of  $\lambda$  ( $\theta_k$ : black line,  $\varepsilon_k$ : red line) of (a, b) Co and (c, d) Ni nanovoids with the same deposition time  $t = 100$  s.

### 3. Results and Discussions

To demonstrate the impact of ferromagnetic material on MOKE signal, Fig. 3 gave out the MOKE spectra for both Co (a, b) and Ni (c, d) nanovoids. The deposition time was fixed as  $t = 100$  s, and the lattice of the nanovoids array were  $\Lambda = 530$  nm (a, c) and  $620$  nm (b, d), respectively. There was one prominent structure dominated the spectrum of every sample, furthermore, the location of the prominent structure was fixed near  $\lambda = 465$  (a) and  $480$  nm (c) for samples with lattice  $\Lambda = 530$  nm, and located near  $\lambda = 534$  (b) and  $558$  nm (d) for samples with lattice  $\Lambda = 620$  nm, respectively. Obviously, resonant location of Ni nanovoids (c, d) were slight redshift compared with that of corresponded Co nanovoids. The location of featured structure in MOKE spectra of samples with different lattice (a, c) and (b, d) told that the featured structure were related to their lattice. In Fig. 3 of ref [29], the resonant structure of Co nanovoids with deposition time  $t = 150$  s were located near  $\lambda = 480$  nm and  $\lambda = 557$  nm for lattice  $\Lambda = 530$  nm (a) and  $620$  nm (b), respectively, which were close to that of samples with deposition time  $t = 100$  s with corresponded lattice. Evidently,



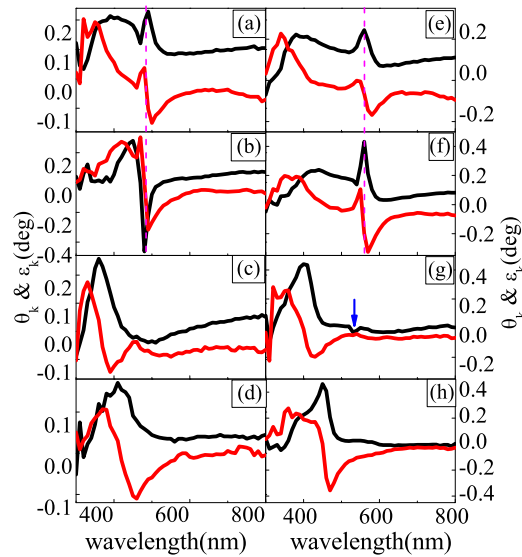


Fig. 4.  $\theta_k$  (black line) and  $\varepsilon_k$  (red line) as function of  $\lambda$  of samples with lattice (a-d)  $\Lambda = 530$  nm and (e-h)  $\Lambda = 620$  nm, respectively. The deposition time  $t = 60, 100, 200,$  and  $300$  s from up to down.

MOKE signals modulated with nanovoids were most related to the configurations of voids. The slightly redshift in Ni nanovoids (c, d) were originated from the different refractive index of Co and Ni. The bandwidth of the featured structure was narrower than that of Co nanovoids (a, b), this might be attributed to the self-passivation properties of Ni [28].

In Ni antidot thin films, the energy shift of the surface plasmon resonance dependent on the hole-size had been studied [30], where with fixed lattice  $a = 920$  nm, a red shift of the peaks position was exhibited with varying the hole size from 869 nm to 636 nm. The hardly shift of the featured structure here denoted slight varying of the outermost lateral diameter of the nanovoids, which could be attributed to the slowly changing of the outermost lateral radius of the voids when radial depth was close to the radius of spheres. With enlarging the deposition time, both radial depth and the lateral outermost diameter of nanovoids changed coordinately, as could be seen in Fig. 2, which would render novel properties presented in MOKE signal.

The measured spectra of polar Kerr rotation  $\theta_k$  (black line) and ellipticity  $\varepsilon_k$  (red line) versus wavelength  $\lambda$  of fabricated samples with different deposition time were layered out in Fig. 4. The depth of voids were corresponded to Table 1(a)–(d) for lattice  $\Lambda = 530$  nm and Table 2(e)–(h) for  $\Lambda = 620$  nm with  $t = 60$  s (a e), 100 s (b f), 200 s (c g), and 300 s (d h), respectively. As could be seen, one prominent featured structure dominated  $\theta_k$  and  $\varepsilon_k$  spectra of every samples, and were blue-shifted with deepening of voids, which located near wavelength  $\lambda = 484, 480, 361,$  and  $439$  nm for samples with  $\Lambda = 530$  nm, and  $\lambda = 558, 558, 403,$  and  $450$  nm for samples with  $\Lambda = 620$  nm, respectively. For samples with depth not surpass the half diameter, the featured structures were almost fixed at the location  $\lambda \approx 480$  nm for samples with  $\Lambda = 530$  nm (a, b), and  $\lambda \approx 558$  nm for samples with  $\Lambda = 620$  nm (e, f), as denoted by the dashed purple line. The physical mechanism of these featured structures was ascribed to hybrid optical modes of surface lattice resonance and nanocavity modes [29]. When the depths were close to or surpassed radius of spheres, intensive blue shift of the featured structure in MOKE spectra were demonstrated, as can be seen in Fig. 4(c), (d) and (g), (h), due to the rim dipole modes occurred, strong enhanced fields localized in individual nanovoid [31], [32]. The blue shifts were larger for samples with deposition time  $t = 200$  s (c, g) than 300 s (d, h), which could be ascribed to the enlarged lateral outermost radius of sample with deposition time  $t = 200$  s (c, g) than that of samples with deposition time  $t = 300$  s (d, h) [30]. The half-bandwidth of  $\theta_k$  peaks in Fig. 4(c), (d) and (g), (h) became broadened due to high absorption of more ferromagnetic materials Ni included with enlarging the deposition time.

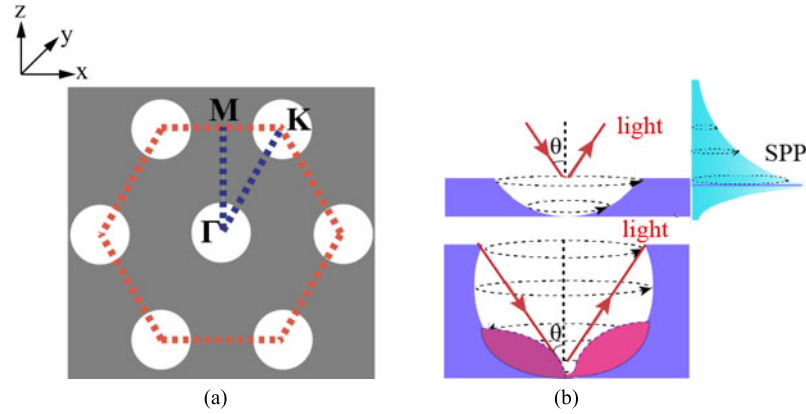


Fig. 5. Schematic plot of (a) the first Brillouin zone of hexagonal structure and (b) the flux of SPP under x-polarization.

To further study the physical mechanism of MOKE signal, angle-resolved spectroscopy (ARPS) detection were performed to analyze the optical modes in these nanostructures. ARPS was powerful analysis technique in the realm of optical nanostructures. As indicated in Fig. 5(a) and (b), supposing the light impinged on the sample in the  $xz$ -plane under TM-polarization (with magnetic field perpendicular to  $xz$ -plane), the magnetic field in the semi-space can be written as

$$H_y(\vec{r}, z) = \delta_{m,0} e^{-ik_{zm}z} e^{ik_x x} + \sum_m r_m e^{ik_{zm}z} e^{i(k_x + 2\pi m/\Lambda)x} \quad (1)$$

Where the first part in right side denotes the incident plane wave with  $\delta_{m,0}$  being the Kronecker function and  $m$  being the Bloch order,  $e^{i(k_x + 2\pi m/\Lambda)x}$  denotes the wave component of the  $m$ th Bloch eigenmode. The optical modes (OM) are related mostly to the wavevector in both  $x$ - and  $y$ -direction. Here, the wavevector of SPP or other optical mode can be written as [15]:

$$\vec{K}_{SPP/OM} = 2\pi/\lambda \sin \theta \pm \vec{G}_x \pm \vec{G}_y \quad (2)$$

Where the first part in the right is in-plane momentum of the incident light with an incidence angle  $\theta$ ,  $\vec{G}_x$  and  $\vec{G}_y$  represent the reciprocal lattice along  $x$ - and  $y$ -direction. In case of 2D hexagonal lattice as denoted in Fig. 5(a), where  $|\vec{G}_x| = |\vec{G}_y| = \frac{4\pi}{\sqrt{3}\Lambda}$ , we get:

$$\vec{K}_{SPP/OM} = \sqrt{k_0^2 \sin^2 \theta \pm \frac{4\pi^2}{\Lambda^2} k_0 (n + m) \sin \theta + \frac{4\pi^2}{\Lambda^2} \left( \frac{4}{3} (n^2 + m^2 + mn) \right)} \quad (3)$$

Here,  $\Lambda$  is the lattice constant of the periodic array, and the integer  $n$  and  $m$  denote the order of resonance. In the normal incidence, the resonance wavelength can be described as:

$$\lambda = \text{Re} \left( \frac{\Lambda}{\sqrt{\frac{4}{3} (n^2 + m^2 + mn)}} \sqrt{\frac{\varepsilon_m \varepsilon_d}{\varepsilon_m + \varepsilon_d}} \right) \quad (4)$$

$\varepsilon_m$  and  $\varepsilon_d$  represent the dielectric permittivity of metal and dielectric, respectively. The solutions of eq. (4) denote the resonance wavelength of surface lattice resonance due to SPP diffracted by the lattice of the voids. As indicated in Fig. 5(a), under TM-polarization, when changing the incident angle  $\theta$  in experiment, the evolution of the reflection dips along the Gamma-M direction (Fig. 5(a)) of the hexagonal reciprocity lattice can be acquired. Changing the polarization of the incident light from TM to TE, the evolution of the reflection dips along K-Gamma can be gained with varied incident angle  $\theta$  [33].

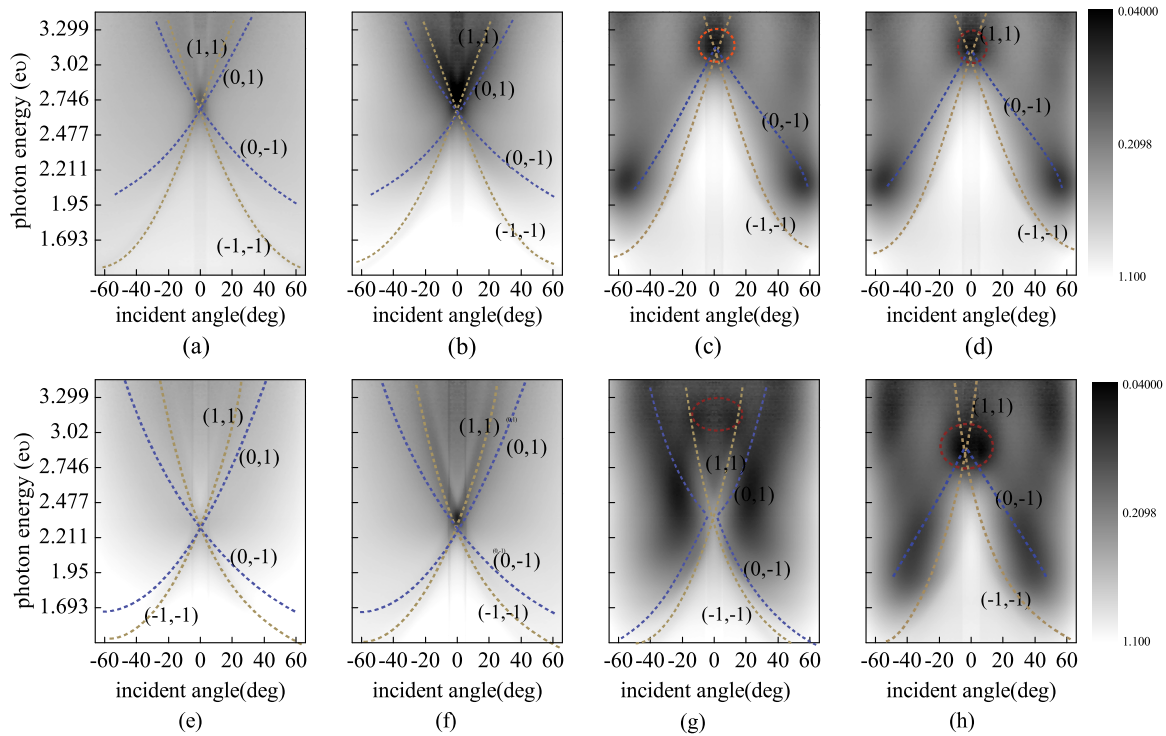


Fig. 6. Angle-resolved reflective spectra a function of  $\lambda$  of samples with lattice (a–d)  $\Lambda = 530$  nm and (e–h) 620 nm. The deposition time  $t = 60, 100, 200,$  and  $300$  s from left to right.

Fig. 6 gave out the angle-resolved reflective spectra of samples with lattice  $\Lambda = 530$  nm (a–d) and 620 nm (e–h), for samples with deposition time  $t = 60, 100, 200, 300$  s from left to right. The incident light were unpolarised, that is to say, the spectra in Fig. 6 were superimposed data with polarization of TM and TE. For clarity, the diffraction order of Bragg plasma were marked out with reciprocal vector  $(m, n)$ , and the evolution were denoted by the dashed line in Fig. 6 for all samples. At  $\theta = 0^\circ$ , degeneracy points were revealed in the angle resolved spectra near photon energy  $E \approx 2.62$  (a), 2.62 (b), 3.12 (c), 3.08 (d) in the unit of  $eV$  for samples with  $\Lambda = 530$  nm, and  $E \approx 2.25$  (e), 2.25 (f), 2.25 (g), and 2.79 (h) in the unit of  $eV$  for samples with  $\Lambda = 620$  nm. The location of degeneracy point corresponded to that of peaks in  $\theta_k$  spectra in Fig. 4 well. Therefore, the mode information offered by ARPS could be used to elucidate the origin of MOKE signal. For shallow voids in Fig. 2(a), (b) and (e), (f), as indicated by the schematic plot in Fig. 5(b) (upper), SPP occurred by the aids of the periodic geometry of nanovoids, and propagated along the  $xy$ -surface. SLR with orders  $(0, 1)$  (the dashed blue line) and  $(1, 1)$  (the dashed dark yellow line) degenerated at  $\Gamma$  point were clearly demonstrated in ARPS in Fig. 6(a), (b) and (e), (f). Besides, weak localized plasmons also contributed to the MOKE signal at normal incident, for that darker zone superimposed with the degeneracy points  $\Gamma$  in Fig. 6(a), (b) and (e), (f), and varied slightly within small incident angle. As results, MOKE signal corresponded in Fig. 4(a), (b) and (e), (f) could be attributed to SLR and weak localized plasmons resonance. With the voids deepened, as indicated in the schematic plot in Fig. 5(b) (down), SPP occurred and localized in the nanovoids, standing waves (light red lobes in (b) (down)) occurred in the deep nanovoids due to the lattice scattering [34], which intensified the interaction of ferromagnetic materials and light. Here, the degeneracy points  $\Gamma$  in Fig. 6(c), (d) and (h) became enlarged and darkened, implying more electromagnetic field were localized in the voids. Besides, the degeneracy points in Fig. 6(c), (d) and (h) were blue-shifted, which were in accord with the blue-shifted  $\theta_k$  peaks in MOKE spectra in Fig. 4 (c), (d) and (h), and in these instances, plasmons localized in the voids dominated MOKE signal. Comparing the outermost diameter of shallow voids



in Fig. 2(a), (b), (e), (f) with that of deep ones in Fig. 2(c), (d), (g), (h), we found that the featured structures in MOKE signal were blue-shifted with the enlarged diameter of the voids, which was different from refs [30]. Thus, we deduced that these blue shifts were mainly dominated by radial depth of the voids, which was related to the localized plasmons occur. Furthermore, the localized plasmons scattered by the geometry of the lattice, the degenerate point of the scattering blue-shifted due to the high effective index of the nanovoids. From ARPS in Fig. 6(g), the degeneracy point in Fig. 6(g) was located still near  $E \approx 2.25$  eV due to the relatively shallow voids compared with that of samples with ARPS in Fig. 6(c), (d) and (h). There was weak featured structure located at the  $\lambda \approx 530$  nm in MOKE signal in Fig. 4(g) as denoted by blue arrow, corresponding to the location of degeneracy point. The prominent featured structure in Fig. 4(g) was located near  $\lambda \approx 558$  nm, and closed to the location of broad dark zone, we could deduce that MOKE signal in Fig. 4(g) was also dominated by localized plasmons. The degeneracy points in Fig. 6(a), (b), (e), (f) and (c), (d), (g), (h) came from different physical mechanism. For that of shallow voids in Fig. 6(a), (b), (e), (f), diffraction of surface plasmons due to the interaction of the geometry and light dominated. And for the deeper ones in Fig. 6(c), (d), (g), (h), the Mie scattering of localized plasmons were main factor, and at large incident angle  $\theta$ , the localized plasmons were scattered parallel to the Bragg lines, this would be discussed in further study.

#### 4. Conclusion

In conclusion, with the aid of nanosphere lithography and electrochemical deposition, ferromagnetic Ni nanovoids with different depths arrayed on noble metal surface were fabricated. Through MOKE properties comparing of Ni nanovoids with that of Co nanovoids, we found that the featured structure in MOKE signal was mainly dominated by the voids configuration, especially the depth of the voids, which might introduce more optical modes. Furthermore, the physical mechanism analysis about these optical modes of these featured structure in MOKE signal were analyzed by the aid of ARPS technique. For shallow nanovoids, MOKE modulation was attributed to SLR, and for deeper ones, localized plasmons in the voids were dominated. For shallow Ni nanovoids samples, narrower bandwidth were demonstrated than that of Co nanovoids, which might be used in high sensitivity biosensors fabrication [29].

#### Acknowledgment

The authors would like thank the support of Soft-X Ray Interference Lithography Beam line (BL08U1B) in SSRF for sample preparation and characterization.

---

#### References

- [1] I. L. Lyubchanskii, N. N. Dadoenkova, M. I. Lyubchanskii, E. A. Shapovalov, and Th. Rasing, "Magnetic photonic crystals," *J. Phys. D, Appl. Phys.*, vol. 36, pp. R277–R287, 2003.
- [2] M. Inoue *et al.*, "Magnetophotonic crystals," *J. Phys. D, Appl. Phys.*, vol. 39, pp. R151–R161, 2006.
- [3] M. Levy, A. A. Jalali, and X. Huang, "Magnetophotonic crystals: Nonreciprocity, birefringence and confinement," *J. Mater. Sci. Mater. Electron.*, vol. 20, pp. 43–47, 2009.
- [4] D. Grundler, "Reconfigurable magnonics heats up," *Nature Phys.*, vol. 11, pp. 438–441, 2015.
- [5] M. Krawczyk and D. Grundler, "Review and prospects of magnonic crystals and devices with reprogrammable band structure," *J. Phys. Condens. Matter*, vol. 26, 2014, Art. no. 123202.
- [6] B. J. H. Stadler and T. Mizumoto, "Integrated magneto-optical materials and isolators: A review," *IEEE Photon. J.*, vol. 6, no. 1, pp. 1–15, Feb. 2014.
- [7] R. Kolkowski, J. Szeszko, B. Dwir, E. Kapon, and J. Zyss, "Non-centrosymmetric plasmonic crystals for second-harmonic generation with controlled anisotropy and enhancement," *Laser Photon. Rev.*, vol. 10, pp. 287–298, 2016.
- [8] V. Clavijo-Jordan, V. D. Kodibagkar, S. C. Beeman, B. D. Hann, and K. M. Bennett, "Principles and emerging applications of nanomagnetic materials in medicine," *Wiley Interdiscipl. Rev., Nanomed. Nanobiotechnol.*, vol. 4, pp. 345–365, 2012.
- [9] A. A. Grunin, I. R. Mukha, A. V. Chetvertukhin, and A. A. Fedyanin, "Refractive index sensor based on magnetoplasmonic crystals," *J. Magnetism Magn. Mater.*, vol. 415, pp. 72–76, 2016.
- [10] N. Maccaferri *et al.*, "Ultrasensitive and label-free molecular-level detection enabled by light phase control in magnetoplasmonic nanoantennas," *Nature Commun.*, vol. 6, 2015, Art. no. 6150.

- [11] P. Fumagalli, C. Spaeth, U. Rudiger, and R. J. Gambino, "A new magneto-optic enhancement effect in macroscopic ferrimagnets," *IEEE Trans. Magn.*, vol. 31, no. 6, pp. 3319–3324, Nov. 1995.
- [12] K. H. J. B. E. P. Wohlfarth, *Ferromagnetic Materials Vol. 5*, Amsterdam, The Netherlands: Elsevier, 1990.
- [13] M. Freiser, "A survey of magneto-optic effects," *IEEE Trans. Magn.*, vol. MAG-4, no. 2, pp. 152–161, Jun. 1968.
- [14] A. V. Butko, A. A. Klimov, S. A. Nikitov, and Y. A. Filimonov, "Using the magneto-optical Kerr effect to study magnetization processes in two-dimensional magnonic crystals based on YIG thin films," *J. Commun. Technol. Electron.*, vol. 51, pp. 944–947, 2006.
- [15] H. Raether, *Surface Plasmons on Smooth and Rough Surfaces and on Gratings*. Berlin Heidelberg: Springer, 1988.
- [16] L. E. Kreilkamp *et al.*, "Waveguide-Plasmon polaritons enhance transverse magneto-optical Kerr effect," *Phys. Rev. X*, vol. 3, 2013, Art. no. 041019.
- [17] E. Ozbay, "Plasmonics merging photonics and electronics at nanoscale dimensions," *Science*, vol. 311, pp. 189–194, 2006.
- [18] N. I. Zheludev, "Obtaining optical properties on demand," *Science*, vol. 348, pp. 973–975, 2015.
- [19] A. Femius Koenderink, A. Alù, and A. Polman, "Nanophotonics shrinking light-based technology," *Science*, vol. 348, pp. 516–522, 2015.
- [20] M. Liu and X. Zhang, "Nano-optics: Plasmon-boosted magneto-optics," *Nature Photon.*, vol. 7, pp. 429–430, 2013.
- [21] G. Armelles, A. Cebollada, A. García-Martín, and M. U. González, "Magnetoplasmonics: Combining magnetic and plasmonic functionalities," *Adv. Opt. Mater.*, vol. 1, pp. 10–35, 2013.
- [22] V. I. Belotelov *et al.*, "Plasmon-mediated magneto-optical transparency," *Nature Commun.*, vol. 4, 2013, Art. no. 2128.
- [23] M. Kataja, T. K. Hakala, A. Julku, M. J. Huttunen, S. van Dijken, and P. Torma, "Surface lattice resonances and magneto-optical response in magnetic nanoparticle arrays," *Nature Commun.*, vol. 6, 2015, Art. no. 7072.
- [24] M. Kataja *et al.*, "Hybrid plasmonic lattices with tunable magneto-optical activity," *Opt. Exp.*, vol. 24, pp. 3652–3662, 2016.
- [25] N. Maccaferri *et al.*, "Resonant enhancement of magneto-optical activity induced by surface plasmon polariton modes coupling in 2D magnetoplasmonic crystals," *ACS Photon.*, vol. 2, pp. 1769–1779, 2015.
- [26] L. Chen *et al.*, "Tunable Fano resonance and magneto-optical response in magnetoplasmonic structure fabricated by pure ferromagnetic metals," *Phys. Rev. B*, vol. 93, 2016, Art. no. 214411.
- [27] L. Shi, T. K. Hakala, H. T. Rekola, J. P. Martikainen, R. J. Moerland, and P. Törmä, "Spatial coherence properties of organic molecules coupled to plasmonic surface lattice resonances in the weak and strong coupling regimes," *Phys. Rev. Lett.*, vol. 112, 2014, Art. no. 153002.
- [28] E. T. Papaioannou *et al.*, "Surface plasmons and magneto-optic activity in hexagonal Ni anti-dot arrays," *Opt. Exp.*, vol. 19, pp. 23867–23877, 2011.
- [29] X. Zhang *et al.*, "Resonant magneto-optical Kerr effect induced by hybrid plasma modes in ferromagnetic nanovoids," *Chin. Phys. B*, vol. 26, 2017, Art. no. 117801.
- [30] H. Fang *et al.*, "Observation of a hole-size-dependent energy shift of the surface-plasmon resonance in Ni antidot thin films," *Appl. Phys. Lett.*, vol. 106, 2015, Art. no. 153104.
- [31] C. Michael and F. Mike, "A plasmon-induced current loop in gold semi-shells," *Nanotechnology*, vol. 18, 2007, Art. no. 235704.
- [32] R. M. Cole, J. J. Baumberg, F. J. Garcia de Abajo, S. Mahajan, M. Abdelsalam, and P. N. Bartlett, "Understanding plasmons in nanoscale voids," *Nano Lett.*, vol. 7, pp. 2094–2100, 2007.
- [33] T. Ochiai and K. Sakoda, "Dispersion relation and optical transmittance of a hexagonal photonic crystal slab," *Phys. Rev. B*, vol. 63, 2001, Art. no. 125107.
- [34] T. A. Kelf *et al.*, "Localized and delocalized plasmons in metallic nanovoids," *Phys. Rev. B*, vol. 74, 2006, Art. no. 245415.